SCIENTIFIC REPORTS

OPEN

SUBJECT AREAS:
BATTERIES
CARBON NANOTUBES AND FULLERENES
ELECTRONIC MATERIALS
NANOPARTICLES

Received
16 August 2013

Accepted
12 November 2013

Published
2 December 2013

Correspondence and requests for materials should be addressed to Q.W.C. (cqw@ustc.edu.cn)

Fe_2O_3 Nanoparticles Wrapped in Multi-walled Carbon Nanotubes With Enhanced Lithium Storage Capability

Nan Yan[1], Xuhui Zhou[1], Yan Li[1], Fang Wang[1], Hao Zhong[1], Hui Wang[2] & Qianwang Chen[1]

[1]Hefei National Laboratory for Physical Sciences at Microscale, Department of Materials Science & Engineering & Collaborative Innovation Center of Suzhou Nano Science and Technology, University of Science and Technology of China, Hefei, Anhui 230026, P. R. China, [2]Department of Chemistry, College of Staten Island, and The Graduate Center, The City University of New York, Staten Island, NY 10314, USA.

We have designed a novel hybrid nanostructure by coating Fe_2O_3 nanoparticles with multi-walled carbon nanotubes to enhance the lithium storage capability of Fe_2O_3. The strategy to prepare Fe_2O_3@MWCNTs involves the synthesis of Fe nanoparticles wrapped in MWCNTs, followed by the oxidation of Fe nanoparticles under carbon dioxide. When used as the anode in a Li-ion battery, this hybrid material (70.32 wt% carbon nanotubes, 29.68 wt% Fe_2O_3) showed a reversible discharge capacity of 515 mAhg^{-1} after 50 cycles at a density of 100 mAg^{-1} and the capacity based on Fe_2O_3 nanoparticles was calculated as 1147 mAhg^{-1}, Three factors are responsibile for the superior performance: (1) The hollow interiors of MWCNTs provide enough spaces for the accommodation of large volume expansion of inner Fe_2O_3 nanoparticles, which can improving the stability of electrode; (2) The MWCNTs increase the overall conductivity of the anode; (3) A stable solid electrolyte interface film formed on the surface of MWCNTs may reduce capacity fading.

With a fast-developing technology in electric energy storage, Li-ion batteries (LIBs) have become the predominant power source for portable electronics due to their high energy density, long lifespan and environment benignity[1,2]. Up to now, although great progress have been achieved by using graphite as anode material for commercial LIBs, the lower theoretical capacity (372 mAhg^{-1}) of graphite limits its further practical application[3–5]. Transition metal oxides, as anode materials for LIBs, have gained significant momentum due to their higher theoretical capacities than graphite by the formation of metal simple substance through a chemical conversion mechanism[6,7]. Among these transition metal oxides materials, Fe_2O_3 is believed to be a promising candidate to replace graphite because of its high theoretical capacity (1007 mAhg^{-1}), low cost, ease of fabrication and environmental benignity[8–10]. In principle, the lithium storage capacity of Fe_2O_3 is attributed to the reversible conversion reaction between Li^+ ions and Fe_2O_3, leading to the formation of Fe NPs in a Li_2O matrix. Generally, the conversion reaction will results in fast capacity fading of Fe_2O_3 due to the drastic volume variation and severe destruction of the electrode upon electrochemical cycling. In addition, the low conductivity of Fe_2O_3 also induces additional performance degradation, especially at high current densities[11]. Furthermore, during the cycle process, the solid electrolyte interface (SEI) films formed at the interface between Fe_2O_3 and liquid electrolyte can be broken owing to the shrink of Fe_2O_3 anode materials. When the fresh Fe_2O_3 is exposes to the electrolyte again, the thicker of SEI film will increase with each charge/discharge cycle, which obviously leads to a degradation in battery performance[12]. In order to solve puzzle of Fe_2O_3 anode materials, all kinds of approach including the synthesis of hollow-structured Fe_2O_3 have been attempted[13–15]. Although the hollow structure can provide high surface area, short lithium diffusion length to enhance the rate capacity and extra free space to alleviate the volume variation, it is still a challenge to deal with low conductivity and unstable SEI films of Fe_2O_3 anode materials[16].

Fabrication of hybrid nanomaterials with carbon coating has been considered as one of the most effective ways towards high-performance electrode materials for LIBs, especially for the electrode materials with volume variation during the charge-discharge process[17]. Under the stimulus of their special properties, various carbon-mixed Fe_2O_3 anode materials have been reported[18–21]. Due to their porous structure and execllent electrical conductivity, carbon nanotubes (CNTs) are widely used in the filed of preparation of hybrid electrode materials. For example, Zhou et al. have prepared a nanosized Fe_2O_3 decorated single-walled carbon nanotube (SWCNT) membrane as a high-performance flexible anode for LIBs, showing a discharge capacity of 801 mAhg^{-1} after 90 cycles. The highly conducting SWCNT network in membrane not only facilitates electron conduction of Fe_2O_3, but also buffers the strain of Fe_2O_3[22]. Lou's group have synthesized carbon-coated Fe_2O_3 hollow nanohorns on the CNTs backbone for superior lithium storage capability. The CNTs backbone and the outmost continuous carbon nanocoating may serve as a structural buffering layer to cushion the internal strain. This hybrid nanomaterial demonstrates a discharge capacity of 820 mAhg^{-1} after 100 cycles, while CNT@Fe_2O_3 without carbon coating has a discharge capacity of 660 mAhg^{-1} [23]. In addition to the well conductivity, CNTs have other advantages in the application of electrode for LIBs. The hollow interior of CNTs is an ideal carrier for metal oxide NPs, which could provide enough inner space for the large volume expansion of metal oxide NPs in charge/discharge cycling of batteries. Furthermore, a stable SEI film could be formed during lithiation and delithiation because the electrolyte will contact with the outer surface of CNTs. Therefore, the purpose of this work is to design a novel hybrid material with discontinuous Fe_2O_3 NPs wrapped in MWCNTs and investigated its potential application as an anode material in lithium ion batteries.

Results

Fig. 1 schematically illustrates the procedure to generate Fe_2O_3@MWCNTs. First, Fe@MWCNTs are synthesized by placing dried ferrocene in a vacuum tube, which has been reported by our group[24,25]. Firstly, Fe NPs are generated in the decomposition process of ferrocene, then the chemical bonds of C–H are ruptured and the graphitic shells are formed due to the Fe NPs acting as catalysts[26]. Second, in order to obatin the hybrid nanostructure of Fe_2O_3@MWCNTs, the Fe@MWCNTs were conducted at high temperature (700°C) using carbon dioxide as surrounding environment for oxidation of Fe NPs and for protection of MWCNTs[27]. When used as anode material for LIBs, the Fe_2O_3 NPs react with lithium ions and form Fe NPs in a Li_2O matrix during the discharge process, then reversibly react in the charge process. Owing to the structural stability of MWCNTs and discontinuous distribution of Fe_2O_3 NPs, this volume change of Fe_2O_3 NPs only occurs in the hollow interior of MWCNTs, which can provide the enough inner space for accommodation of the large volume variation. The larger inner space for enhanced lithium storage capability have been confirmed by previous papers including tin-NPs encapsulated in elastic hollow carbon spheres[28], Si NPs encapsulated in continuous hollow carbon tubes[29] and hollow carbon nanofiber-encapsulated sulfur[30]. However, compared with above the amorphous carbon coating, MWCNTs will have a relatively stronger conductivity, which obviously enhance conductivity of Fe_2O_3 as anode materials.

The crystallographic structure of the hybrid material was analyzed by X-ray diffraction (XRD), shown in Fig. 2(a). In black line (Fe@MWCNTs), a relatively strong peak centred at 44.8° and a weak peak centred at 65.2° are observed, which can be indexed as crystalline Fe (110) and (200) diffractions (JCPDF 89-4186), respectively. A weak broadening diffraction peak at 26.3° is well indexed as the (002) reflection of graphite (JCPDF 75-2078). After high temperature oxidation of Fe@MWCNTs using carbon dioxide as oxidant, the sharp diffraction peak at 18.4°, 30.3°, 35.7°, 37.3°, 43.3°, 53.8°, 57.3°, 62.9° can be obviously found, which correspond well to the (111), (220), (311), (222), (400), (422), (511) and (440) crystal planes of iron oxide (JCPDS file 19-0629, Fe_2O_3, or JCPDS file 39-1346, Fe_2O_3), respectively. However, it is hard to identify the iron oxides Fe_3O_4 or gamma-Fe_2O_3 due to their same spinel structure and similar lattice parameter a (0.8346 nm for gamma-Fe_2O_3 and 0.8396 nm for Fe_3O_4)[31]. Simultaneously, the diffraction peaks of Fe disappear and the peak of graphite still remain, which means the completely conversion from Fe@MWCNTs to iron oxide@MWCNTs.

Because of the similar XRD pattern of gamma-Fe_2O_3 and Fe_3O_4, the Raman spectrum was used to further confirm the composition of the hybrid material. Fig. 2(b) shows the Raman spectrum of Fe_2O_3@MWCNTs at the range of 100–1900 cm^{-1}. According to the previous report, the peaks located at 216 cm^{-1}, 280 cm^{-1} and 390 cm^{-1} should result from one A_{1g} mode and two E_g modes of Fe_2O_3, respectively[32]. Meanwhile, compared with standard Fe_2O_3 Raman spectrum, a small blue-shift may attribute to the interaction between Fe_2O_3 and MWCNTs[33]. Moreover, the peak at around 1576 cm^{-1} involves the in-plane bond stretching motion of pairs of carbon sp^2 atoms, which also exists in the G mode with E_{2g} symmetry. The D mode of graphite around 1346 cm^{-1} is related to the degree of disorder in carbon sp^2 bonded clusters in graphite[24]. Therefore, the two peaks indicate the existence of carbon in the products. In addition, the two peaks can be used to evaluate the extent of carbon-containing defects. From the Raman spectrum, it can be seen that the MWCNTs contain graphitic structures and defects, which may be helpful to enhance the diffusion rate of Li$^+$ ions and electronics.

The morphology and microstructure of Fe@MWCNTs were examined by SEM and TEM, shown in Fig. S1 and Fig. S2. As shown in Fig. S1, the as-obtained Fe@MWCNTs display standard 1D nanostructures. The TEM image shown in Fig. S2(a) reveals that Fe@MWCNTs have nanotube structures with discontinuous Fe NPs wrapped in CNTs. When the size of some Fe nanoparticles is larger than the inner diameter of the CNTs, the wrapped parts of CNTs may deform, which can be observed from Fig. S2(a). Moreover, it is interesting to find that these nanotubes have a hemispherical "Fe nanoparticles cap" at each end of the cylinder (Fig. S2(b)), resulting in large number of nanoparticles to be visible within the micrograph field of view[24]. After oxidation, the appearance of Fe_2O_3@MWCNTs had not been changed and remained the 1D nanostructures, which can be clearly seen from the SEM image shown in Fig. 2(c). Furthermore, it can be observed that there are many crevices in the surface of MWCNTs, which is useful to increase the contact area of electrode and electrolyte. The TEM image shown in Fig. 2(d)

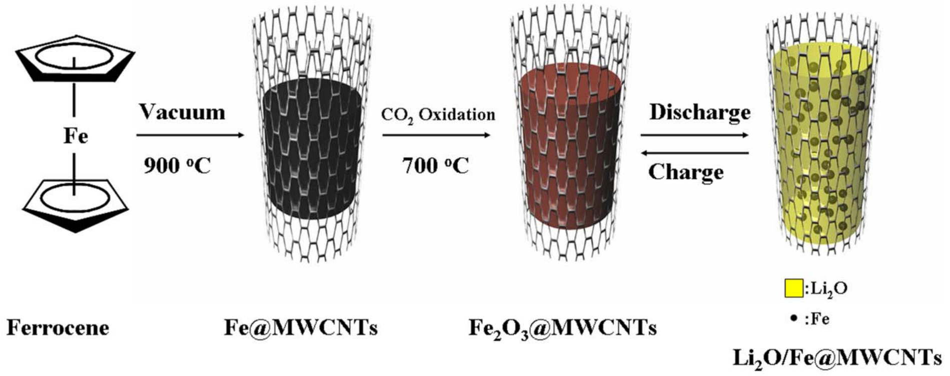

Figure 1 | **Schematic illustration of the formation and discharge/charge process of Fe_2O_3@MWCNTs.**

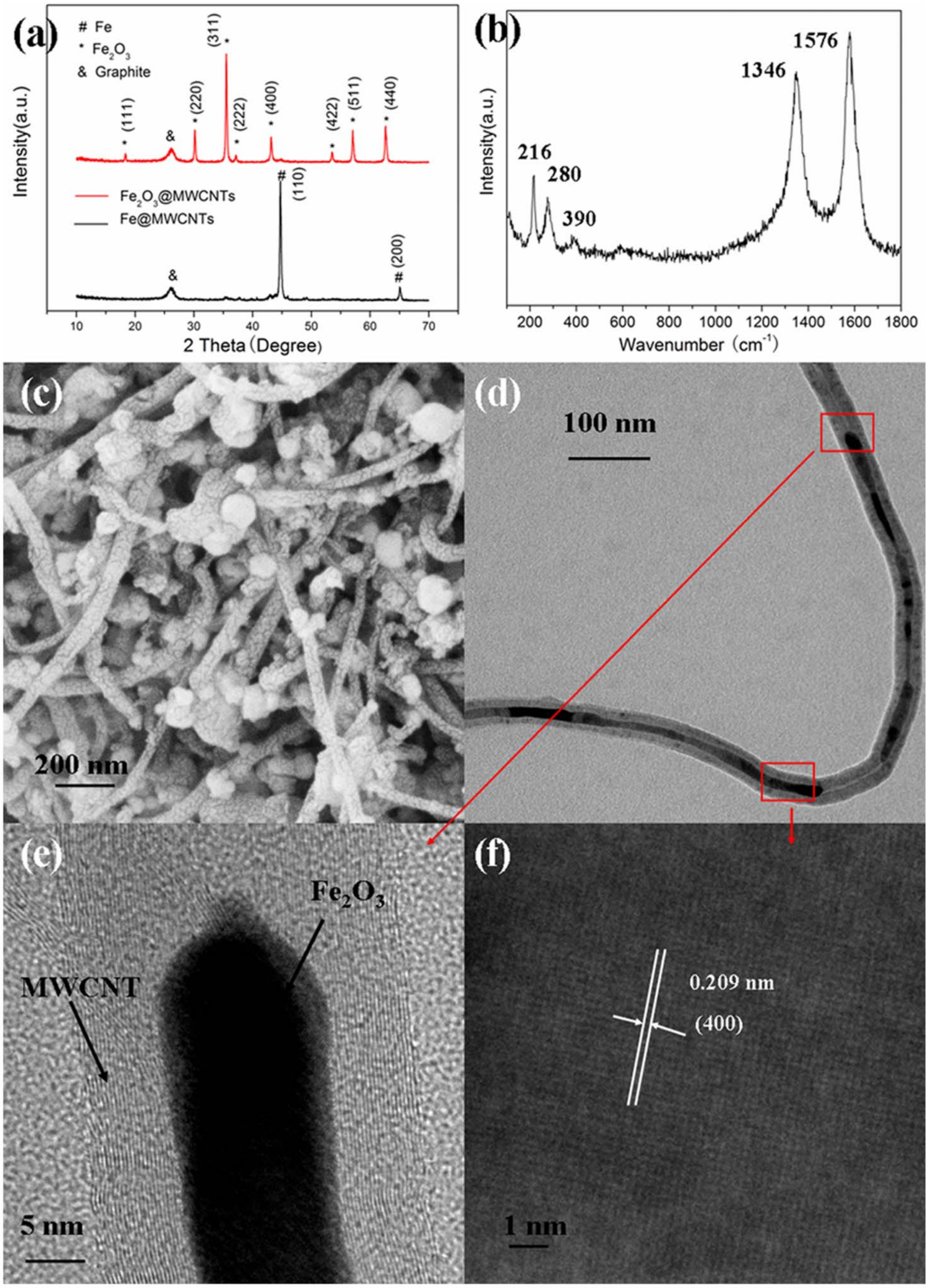

Figure 2 | (a) X-ray diffraction patterns of Fe@MWCNTs and Fe_2O_3@MWCNTs, (b) Raman spectrum of Fe_2O_3@MWCNTs, (c) SEM, (d) TEM and (e–f) HRTEM images of Fe_2O_3@MWCNTs.

illustrates that the Fe_2O_3 NPs are still wrapped in MWCNTs without injuring the wall of MWCNTs. The energy-dispersive X-ray spectrum (Fig. S3) of a single MWCNT indicates the existence of Fe, C and O without other impurity elements. A high-resolution TEM (HRTEM) image shown in Fig. 2(e) clearly demonstrates the graphite layer of carbon nanotube and a 10 nm pore diameter of single MWCNT. Another HRTEM image shown in Fig. 2(f) displays the lattice fringes with a space of 0.209 nm, which can be indexed as (400) lattice plane of Fe_2O_3. The result of the electron microscopy characterization is of good agreement with XRD and Raman characterizations, confirming the successful preparation of Fe_2O_3@MWCNTs.

For further investigation of the chemical composition of the as-prepared Fe_2O_3@MWCNTs, the XPS measurements were carried out. Fig. S4 exhibits a wide scan XPS survey spectrum of Fe_2O_3@MWCNTs between 0 and 1100 eV. The characteristic peaks of C, Fe, and O can be indexed clearly. Meanwhile, the spectrum of Fe 2p is shown in Fig. S5, and the peaks at 710.9 eV and 724.5 eV correspond to the Fe $2p_{3/2}$ and Fe $2p_{1/2}$, respectively[34]. The N_2 absorption/desorption isotherms at 77 K are shown in Fig. S6 and a characteristic of a type IV with type H3 hysteresis loop. The specific surface area calculated with the BET model is 42.55 m^2g^{-1}. The pore size distribution (Fig. S7) has a relatively wide peak of 10 nm, corresponding well with the previous microscopy findings. The mass fraction of Fe_2O_3 and MWCNTs is 29.68% and 70.32% according to the ICP characterization.

Discussion

To investigate the electrochemical performance of Fe_2O_3@MWCNTs, two-electrode 2032 coin cells with Fe_2O_3@MWCNTs anodes were fabricated with Li metal as the counter electrode. The electrochemical performance of Fe_2O_3@MWCNTs was firstly evaluated by cyclic voltammetry (CV) in the 0–3.0 V voltage window at the scan rate of 0.1 mV s^{-1} (Fig. 3(a)). It is clearly seen from the CV curves that there is a substantial difference between the first and the subsequent cycles. There is obviously one reduction peak in the potential of 0.6 V, which appears only in the first cycle. This peak corresponds to the Li^+ ions insertion into Fe_2O_3 and the formation of Li_2O. The first anodic scan shows an extended peak between 1.6 V and 1.9 V, which corresponds to oxidation of Fe to Fe^{3+} ions to re-form Fe_2O_3. For the second and third curves, a broad reduction peak at 0.85 V is observed, which indicates the reversibility and capacity stability. This broadening is due to the amorphous nature/crystal structure destruction of the electrode material[34]. Fig. 3(b) shows the discharge and charge voltage profiles of different cycles at a current density of 100 mAg^{-1}, in good agreement with the CV measurements. A plateau at 0.75 V can be observed only in the first discharge voltage profile, which means the formation of Fe and Li_2O, corresponding to the peaks in CV curves. In the subsequent discharge profiles, the plateau moves to 0.9 V because of the change of crystalline structure in the first cycle[35]. When the discharged electrode has been charged to 3.0 V, a smooth voltage profile is observed until 1.5 V which is followed by sloping voltage plateau up to 2.0 V and a steep rise up to 3.0 V, implying the regeneration of Fe_2O_3. The discharge and charge capacities of the 1st cycle are 870 and 573 $mAhg^{-1}$, respectively, with an initial coulombic efficiency of 65.9%. The discharge capacity of the 2nd cycle is 580 $mAhg^{-1}$. Such an irreversible capacity (290 $mAhg^{-1}$) is attributed to the formation of SEI layer and irreversible electrochemical reactions between lithium ions and electrode material.

To investigate the impact of unique structure of Fe_2O_3@MWCNTs on lithium storage capability, the coin cells based on MWCNTs, commercial Fe_2O_3, the composite of Fe_2O_3 and MWCNTs (same mass ratio with Fe_2O_3@MWCNTs) have been assembled and test under the same condition with Fe_2O_3@MWCNTs. The curves of capacity versus cycle number at a current density of 100 mAg^{-1} were shown in Fig. 3(c). Compared with the contrast, Fe_2O_3@MWCNTs exhibited a reasonable cycle performance. Despite the capacity decayed in the first cycle, even after 50 cycles, the discharge capacity can retain a value of 515 $mAhg^{-1}$. Simultaneously, the initial coulombic efficiency of 47% recovered to 96% in the second cycle, and maintained almost 95% in the subsequent cycles (Fig. S8). As a comparison, MWCNTs, commercial Fe_2O_3 and the composite only exhibited the 50th discharge capacities of 248 $mAgh^{-1}$, 130 $mAhg^{-1}$ and 192 $mAhg^{-1}$, respectively. Although the discharge capacity of Fe_2O_3@MWCNTs is not larger than the previous reports of Fe_2O_3/CNTs composite anode owing to the relatively low loading ratio of Fe_2O_3 nanoparticles. However, according to the discharge capacity (Fe_2O_3@MWCNTs: 515 $mAhg^{-1}$, MWCNTs: 248 $mAhg^{-1}$) and mass ratio (Fe_2O_3: 29.68%, MWCNTs: 70.32%), the discharge capacity contributed by Fe_2O_3 NPs can be calculated as 1147 $mAhg^{-1}$ (Fig. S9), which is higher than the previous reports[8–11,13–15,18–21]. This high value is even larger than the theoretical capacity of Fe_2O_3 (1007 $mAhg^{-1}$), suggesting that such a MWCNTs wrapping structure can enhance the lithium storage capability of Fe_2O_3 and ensure the complete reaction between Fe_2O_3 and Li^+ ions. As mentioned above, Fe_2O_3 NPs react with Li^+ ions and cause volume change inside MWCNTs.

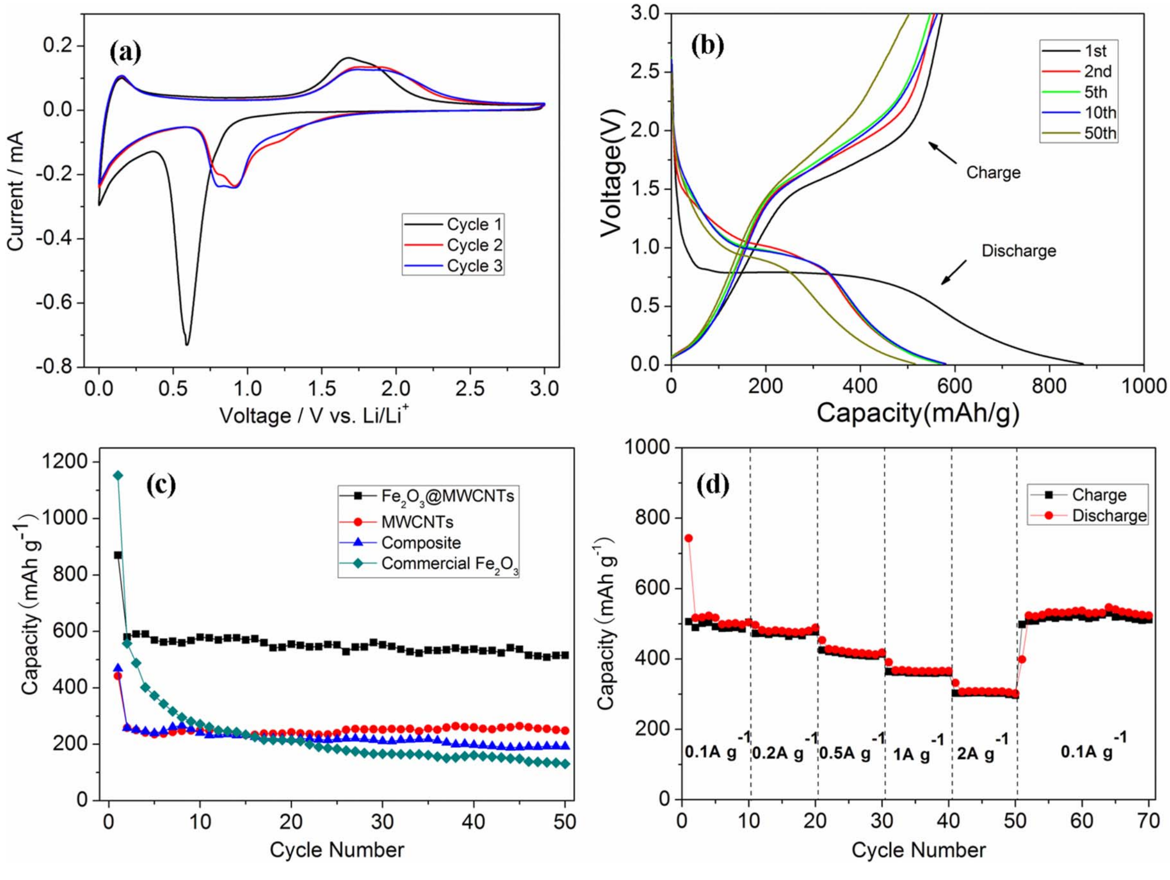

Figure 3 | (a) Cyclic voltammetry of Fe_2O_3@MWCNTs between 3 and 0 V at a scan rate of 0.1 mVs^{-1}, (b) Galvanostatic discharge/charge voltage profiles of Fe_2O_3@MWCNTs at a current density of 100 mAg^{-1}, (c) Discharge capacities versus cycle number of Fe_2O_3@MWCNTs, MWCNTs, the composite and commercial Fe_2O_3 at the current density of 100 mAg^{-1} between 3 and 0 V, (d) Discharge and charge capacity of Fe_2O_3@MWCNTs at different current densities between 3 and 0 V.

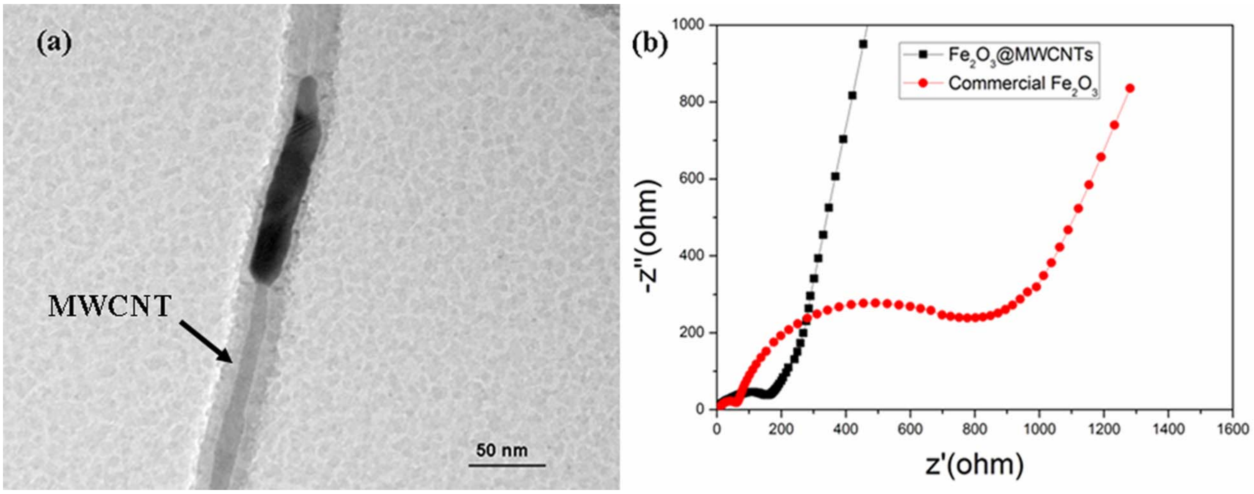

Figure 4 | (a) TEM image of the Fe_2O_3@MWCNTs after 50 cycles, (b) Nyquist plots of ac impedance spectra of Fe_2O_3@MWCNTs and commercial Fe_2O_3.

Furthermore, a stable SEI film can form in the outside of MWCNTs. Thus, Fe_2O_3@MWCNTs exhibits higher and more stable lithium storage capability than commercial Fe_2O_3 and the composite. Although the commercial Fe_2O_3 shows a high initial discharge capacity of 1152 $mAhg^{-1}$, the capacity suffers a fast fading in the following cycles. When tested at the current density of 500 mAg^{-1}, Fe_2O_3@MWCNTs also delivered a discharge capacity of 430 $mAgh^{-1}$ after 40 cycles (Fig. S10), which is better than that for commercial graphite anodes.

In addition to the cycling performance, the high-rate capability is also important especially for high-power applications. Benefited from the unique hybrid structure, the Fe_2O_3@MWCNTs exhibited an excellent rate performance which is shown in Fig. 3(d). Even cycled at a high rate of 2000 mAg^{-1} (3.6 C), this material can still deliver an average discharge of 320 $mAhg^{-1}$. When the current rate is restored to 100 mAg^{-1}, a stable capacity of 520 $mAhg^{-1}$ is resumed.

For revealing the structural evolution of Fe_2O_3@MWCNTs, the electrode after 50 cycles was examined by TEM, which is shown in Fig. 4(a). The structure of a single MWCNT is well preserved, implying the excellent stability of the graphite wall. It has been reported that CNTs can enhance the electrical conductivity transition metal oxide[36]. Because of the existence of large amount of MWCNTs, Fe_2O_3@MWCNTs exhibit much lower resistance than the bare Fe_2O_3, as evidenced by the drastically reduced diameter of the semicircle at high-frequency region in the electrochemical impedance spectroscopy (EIS) patterns (Fig. 4(b)). Moreover, Waki's group has proven that the defects on MWCNTs had positive effects on Li storage property[37]. According to the Raman spectrum shown in Fig. 2b, there is a sharp peak of D mode of graphite around 1346 cm^{-1} which is related to the degree of disorder in carbon sp^2 bonded clusters in graphite. This confirms that MWCNTs have a large amount of defects such as graphitic edges and disordered structures. From the SEM image in Fig. 2c, it can also be seen some crevices in the surface of MWCNTs, which are useful for the accessing of electrolyte into the hollow interior of MWCNTs. Thus the Li^+ ions diffusion and electron transfer are also facilitated to give the greatly enhanced electrochemical performance of Fe_2O_3@MWCNTs. Besides, the synergistic effect between Fe_2O_3 and MWCNTs, for example, storing Li^+ ions in the interface between Fe_2O_3 and MWCNTs, can also enhance the discharge capacity.

In summary, we have designed and synthesized a novel hybrid nanomaterial of Fe_2O_3 NPs wrapped in multi-walled carbon nanotubes. This hybrid nanostructure exhibits a discharge capacity of 515 $mAhg^{-1}$, after 50 cycles as anode electrode for LIBs, while the capacity is calculated as 1147 $mAhg^{-1}$ based on the mass ratio of Fe_2O_3 NPs. Such an enhanced property could be attributed to the unique structure of MWCNTs wrapping, which not only accommodates the large volume variation but also enhances the overall conductivity. Moreover, a stable SEI film formed on the surface of MWCNTs also reduces capacity fading. This hybrid structure can be also applied to enhancing other electrode materials.

Methods

Synthesis. All chemicals are of analytical grade and used without purification. The synthesis of Fe_2O_3 nanoparticles wrapped in multi-walled carbon nanotubes (Fe_2O_3@MWCNTs) contains two steps: Synthesis of Fe nanoparticles wrapped in multi-walled carbon nanotubes (Fe@MWCNTs) and Oxidation of Fe nanoparticles to Fe_2O_3 nanoparticles. The synthesis method of Fe@MWCNTs has been reported by our group[24]. In a typical synthesis, dried ferrocene (0.02 g) were placed into a quartz tube with the inner diameter of 12 mm and effective heating length 150 mm. After being vacuumed, the quartz tube containing ferrocene was sealed. After that, the quartz tube was placed into a tube furnace and heated to 200°C and maintained for 1 h so that the ferrocene can be slowly sublimed in the quartz tube. Subsequently, in order to gradually decompose ferrocene inthe quartz tube, the tube furnace was heated to and maintainedat 400°C for 1 h. Finally, the tube furnace was heated to and maintained at 950°C. After 4 h, the tube furnace was naturally cooled to room temperature. After breaking the quartz tube and intense sonication for 30 min in a beaker, a black solution was obtained and the black products were collected under the induction of a magnet with 0.20 T and washed with ethanol for three times. Then the as-prepared Fe@MWCNTs were oxidized to Fe_2O_3@MWCNTs using carbon dioxide. The annealing process in carbon dioxide was performed at 700°C for 30 min with a heat rate of 10°C min^{-1} to obtain Fe_2O_3@MWCNTs.

Characterization. The powder X-ray diffraction (XRD) patterns were collected on a Japan Rigaku D/MAX-cA X-ray diffractometer equipped with Cu Ka radiation over the 2θ range of 10–80°. Scanning electron microscopy (SEM) images were performed on a JEOL JSM-6700M scanning electron microscope. Transmission electron microscopy (TEM) images were obtained on a Hitachi H-800 transmission electron microscope, using an accelerating voltage of 200 kV. High-resolution transmission electron microscopy (HRTEM) images was taken on a JEOL-2010 transmission electron microscope, which was operated at 200 kV. Energy-dispersive X-ray (EDX) analysis was obtained with an EDAX detector installed on the same HRTEM. The Raman spectrum was taken on a LABRAM-HR Confocal Laser Micro-Raman spectrometer using an Ar^+ laser with 514.5 nm at room temperature. X-ray Photoelectron Spectrum (XPS) was performed on an ESCALAB 250 X-ray Photoelectron Spectrometer with Al Ka radiation. Specific surface areas were calculated from the results of N_2 physisorption at 77 K (Micromeritics ASAP 2020) by using the BET (Brunauer–Emmet–Teller) and BJH (Barrett–Joyner–Halenda). 1 mg Fe_2O_3@MWCNTs was dissolved in 50 mL hydrochloric acid (concentration: 1 $molL^{-1}$). After intense sonication for 10 min, the mixed solution was transferred into a 75 mL Teflon-lined stainless steel autoclave and maintained at 120°C for 8 h and then naturally cooled to room temperature. After centrifuging, the concentration of iron ions in solution was measured using indictive coupled plasma-atomic emission spectroscopy (Atomscan Advantage).

Electrochemical measurements. The electrochemical behavior of the as-prepared Fe_2O_3@MWCNTs was examined using CR2032 coin type cells vs. Li with 1 M LiPF6 in ethylene carbonate and diethyl carbonate (EC:DEC = 1 : 1, v/v) as the electrolyte. The working electrode was fabricated by compressing a mixture of the active materials, conductive material (acetylene black), and binder (polyvinylidene fluoride) in a weight ratio of Fe_2O_3@MWCNTs/carbon/PVDF = 7 : 1 : 2 onto a copper foil current collector, then drying at 60°C for 12 h. The cells were assembled in an argon-filled glove box (MBraun Labmaster 130). The electrode capacity was measured by a galvanostatic discharge-charge method in the voltage range between 3 V and 0 V at a current density of 100 mA g^{-1} on a battery test system (Neware CT-3008W). Cyclic voltammetry was performed using an electrochemical workstation (CHI 660C) between 0–3 V at a scan rate of 0.1 mVs^{-1}. The impedance spectra of the cells were measuredon an electrochemical workstation (CHI 660C) in the frequency range of 0.001–100 kHz.

1. Armand, M. & Tarascon, J.-M. Building better batteries. *Nature* **451**, 652–657 (2008).
2. Bruce, P. G., Scrosati, B. & Tarascon, J. M. Nanomaterials for rechargeable lithium batteries. *Angew. Chem. Int. Ed.* **47**, 2930–2946 (2008).
3. Goodenough, J. B. & Kim, Y. Challenges for rechargeable Li batteries. *Chem. Mater.* **22**, 587–603 (2009).
4. Ji, L. W., Lin, Z., Alcoutlabi, M. & Zhang, X. W. Recent developments in nanostructured anode materials for rechargeable lithium-ion batteries. *Energy Environ. Sci.* **4**, 2682–2699 (2011).
5. Yan, N. *et al.* Hollow Porous SiO_2 Nanocubes Towards High-performance Anodes for Lithium-ion Batteries. *Sci. Rep.* **3**, 1568; DOI:10.1038/srep01568 (2013).
6. Poizot, P., Laruelle, S., Grugeon, S., Dupont, L. & Tarascon, J.-M. Nano-sized transition-metal oxides as negative-electrode materials for lithium-ion batteries. *Nature* **407**, 496–499 (2000).
7. Yan, N. *et al.* Co_3O_4 nanocages for high-performance anode material in lithium-ion batteries. *J. Phys. Chem. C* **116**, 7227–7235 (2012).
8. Wu, C. Z., Yin, P., Zhu, X., Ouyang, C. Z. & Xie, Y. Synthesis of hematite (r-Fe_2O_3) nanorods: diameter-size and shape effects on their applications in magnetism, lithium ion battery, and gas sensors. *J. Phys. Chem. B* **110**, 17806–17812 (2006).
9. Chaudhari, S. & Srinivasan, M. 1D hollow a-Fe_2O_3 electrospun nanofibers as high performance anode material for lithium ion batteries. *J. Mater. Chem.* **22**, 23049–23056 (2012).
10. Zhang, L., Wu, H. B., Madhavi, S., Hng, H. H. & Lou, X. W. Formation of Fe_2O_3 Microboxes with Hierarchical Shell Structures from Metal−Organic Frameworks and Their Lithium Storage Properties. *J. Am. Chem. Soc.* **134**, 17388–17391 (2012).
11. Xu, X. D., Cao, R., Jeong, S. & Cho, J. Spindle-like Mesoporous α-Fe_2O_3 Anode Material Prepared from MOF Template for High-Rate Lithium Batteries. *Nano Lett.* **12**, 4988–4991 (2012).
12. Wu, H. *et al.* Stable cycling of double-walled silicon nanotube battery anodes through solid-electrolyte interphase control. *Nat. Nanotech.* **7**, 310–315 (2012).
13. Wang, B., Chen, J. S., Wu, H. B., Wang, Z. Y. & Lou, X. W. Quasiemulsion-templated formation of α-Fe_2O_3 hollow spheres with enhanced lithium storage properties. *J. Am. Chem. Soc.* **133**, 17146–17148 (2011).
14. Kim, H. S., Piao, Y. Z., Kang, S. H., Hyeon, T. & Sung, Y. E. Uniform hematite nanocapsules based on an anode material for lithium ion batteries. *Electrochem. Commun.* **12**, 382–385 (2010).
15. Kang, N. *et al.* Nanoparticulate iron oxide tubes from microporous organic nanotubes as stable anode materials for lithium ion batteries. *Angew. Chem. Int. Ed.* **57**, 6626–6630 (2012).
16. Wang, Z. Y., Zhou, L. & Lou, X. W. Metal oxide hollow nanostructures for lithium-ion batteries. *Adv. Mater.* **24**, 1903–1911 (2012).
17. Wu, Z. S. *et al.* Graphene/metal oxide composite electrode materials for energy storage. *Nano Energy* **1**, 107–131 (2012).
18. Han, F. *et al.* Nanoengineered polypyrrole-coated Fe_2O_3@C multifunctional composites with an improved cycle stability as lithium-ion anodes. *Adv. Funct. Mater.* **23**, 1692–1700 (2013).
19. Li, Y. *et al.* Simple fabrication of a Fe_2O_3/carbon composite for use in a high-performance lithium ion battery. *Carbon* **52**, 565–573 (2013).
20. Ji, L. W. *et al.* α-Fe_2O_3 nanoparticle-loaded carbon nanofibers as stable and high-capacity anodes for rechargeable lithium-ion batteries. *Appl. Mater. Interfaces.* **4**, 2672–2679 (2012).
21. He, C. N. *et al.* Carbon-encapsulated Fe_3O_4 nanoparticles as a high-rate lithium ion battery anode material. *ACS. Nano* **7**, 4459–4469 (2013).
22. Zhou, G. M. *et al.* A nanosized Fe_2O_3 decorated single-walled carbon nanotube membrane as a high-performance flexible anode for lithium ion batteries. *J. Mater. Chem.* **22**, 17942–17946 (2012).
23. Wang, Z. Y., Luan, D. Y., Madhavi, S., Hu, Y. & Lou, X. W. Assembling carbon-coated α-Fe_2O_3 hollow nanohorns on the CNT backbone for superior lithium storage capability. *Energy Environ. Sci.* **5**, 5252–5256 (2012).
24. Wang, H. *et al.* Fe nanoparticle-functionalized multi-walled carbon nanotubes: one-pot synthesis and their applications in magnetic removal of heavy metal ions. *J. Mater. Chem.* **22**, 9230–9236 (2012).
25. Deng, D. H. *et al.* Iron encapsulated within pod-like carbon nanotubes for oxygen reduction reaction. *Angew. Chem. Int. Ed.* **52**, 371–375 (2013).
26. Hou, H. Q., Schaper, A. K., Weller, F. & Greiner, A. Carbon nanotubes and spheres produced by modified ferrocene pyrolysis. *Chem. Mater.* **14**, 3990–3994 (2002).
27. Ren, S. H., Prakash, R., Wang, D., Chakravadhanula, V. S. K. & Fichtner, M. Fe_3O_4 anchored onto helical carbon nanofibers as high-performance anode in lithium-ion batteries. *ChemSusChem.* **5**, 1397–1400 (2012).
28. Zhang, W. M. *et al.* Tin-nanoparticles encapsulated in elastic hollow carbon spheres for high-performance anode material in lithium-ion batteries. *Adv. Mater.* **20**, 1160–1165 (2008).
29. Wu, H. *et al.* Engineering empty space between Si nanoparticles for lithium-ion battery anodes. *Nano Lett.* **12**, 904–909 (2012).
30. Zheng, G. Y., Yang, Y., Cha, J. J., Hong, S. S. & Cui, Y. Hollow carbon nanofiber-encapsulated sulfur cathodes for high specific capacity rechargeable lithium batteries. *Nano Lett.* **11**, 4462–4467 (2011).
31. Thewlis, J. The structure of ferromagnetic ferric oxide. *J. Philos. Mag.* **12**, 1089–1106 (1931).
32. Faria, D. L. A. D., Silva, S. V. & Oliveira, M. T. D. Raman microspectroscopy of some iron oxides and oxyhydroxides. *J. Raman Spectrosc.* **28**, 873–878 (1997).
33. Teng, X. W., Black, D., Watkins, N. J., Gao, Y. L. & Yang, H. Platinum-maghemite core-shell nanoparticles using a sequential synthesis. *Nano Lett.* **3**, 261–264 (2003).
34. Cherian, C. T. *et al. J. Mater. Chem.* **22**, 12198–12204 (2012).
35. Jin, B. *et al.* Fe_3O_4–pyrolytic graphite oxide composite as an anode material for lithium secondary batteries. *Electrochimica Acta.* **90**, 426–432 (2013).
36. Yin, W. J. *et al.* Origin of bonding between the SWCNT and the Fe_3O_4(001) surface and the enhanced electrical conductivity. *J. Phys. Chem. Lett.* **2**, 2853–2858 (2011).
37. Oktaviano, H. S., Yamada, K. & Waki, K. Nano-drilled multiwalled carbon nanotubes: characterizations and application for LIB anode materials. *J. Mater. Chem.* **22**, 25167–25173 (2012).

Acknowledgments

This work was supported by the National Natural Science Foundation (NSFC, U1232211, 21071137) and Foundation of National Science Base (20772188).

Author contributions

Q.W.C. and N.Y. designed the research, analysed data and wrote the paper. N.Y. and X.H.Z. carried out the electrochemical and physical measurements. H.Z., Y.L., F.W. and H.W. performed electrochemical measurements and other characterization.

Additional information

Supplementary information accompanies this paper at http://www.nature.com/scientificreports

Competing financial interests: The authors declare no competing financial interests.

How to cite this article: Yan, N. *et al.* Fe_2O_3 Nanoparticles Wrapped in Multi-walled Carbon Nanotubes With Enhanced Lithium Storage Capability. *Sci. Rep.* **3**, 3392; DOI:10.1038/srep03392 (2013).